Small

NANO · MICRO small
www.small-journal.com

RESEARCH ARTICLE OPEN ACCESS

Seeded Growth of Plasmonic Core-Shell NU-1000 NanoMOFs With Intracellular Optical Readout

Manuel Ceballos[1] | Oleg Semyonov[1,2] | Enrica Soprano[1] | Ethan Kensett[2] | José Manuel Vila-Fungueiriño[1] | Timothy M. Craig[3] | Sara Bals[3] | Ester Polo[1] | Beatriz Pelaz[1] | Pablo del Pino[1]

[1]Centro Singular de Investigación en Química Biolóxica e Materiais Moleculares (CiQUS), Departamento de Física de Partículas, Universidade De Santiago de Compostela, Santiago de Compostela, Spain | [2]AMOLF, Amsterdam, The Netherlands | [3]EMAT and NANOlight Center of Excellence, University of Antwerp, Antwerp, Belgium

Correspondence: Beatriz Pelaz (beatriz.pelaz@usc.es) | Pablo del Pino (pablo.delpino@usc.es)

Received: 29 April 2026 | **Revised:** 11 July 2026 | **Accepted:** 4 August 2026

Keywords: hyperspectral microscopy | MOFs | nanocomposites | NU-1000 | plasmonics

ABSTRACT

Plasmonic gold bipyramids (AuBipy) encapsulated within a NU-1000 metal-organic framework (MOF) create robust core–shell nanocomposites. These porous nanoassemblies combine the near-infrared (NIR) plasmonic resonance of the metallic core with the intrinsic photoluminescence of the pyrene-based organic linkers. Comprehensive optical characterization reveals efficient photothermal heating under NIR irradiation and robust surface-enhanced Raman scattering (SERS) capabilities in colloidal dispersions. For biological applications, AuBipy@NU-1000 nanocomposites exhibit good colloidal stability and maintain high cell viability in A549 cells up to a 200 pM particle concentration (equivalent to 152 μM of Au and 302 μM of Zr). Wide-field hyperspectral microscopy enables label-free intracellular mapping of the distinct optical signatures of both components after cellular internalization. Spatial analysis of these signals supports preservation of the core-shell architecture inside cells. Consequently, these nanomaterials provide a versatile platform for intracellular optical readout, with additional potential for chemical sensing and photothermal applications.

1 | Introduction

Since the initial reports of MOF-5 and HKUST-1 in 1999 [1, 2], the field of metal-organic frameworks (MOFs) has evolved into a highly tunable class of crystalline porous materials [3]. Their modular combination of inorganic nodes and organic linkers enables precise control over composition, topology, and pore architecture, making them attractive platforms for applications ranging from catalysis to sensing and biomedicine [4–8]. The importance of this materials class was further recognized by the 2025 Nobel Prize in Chemistry, awarded jointly to Susumu Kitagawa, Richard Robson, and Omar M. Yaghi for the development of MOFs.

This structural versatility arises from the coordination between secondary building units (SBUs) and organic linkers [9]. Variations in node connectivity and linker geometry determine the resulting framework topology, pore architecture, and chemical accessibility, which are central to the functional behavior of MOFs [10].

Zr-based MOFs are particularly attractive for applications that require chemical and thermal robustness [11]. Their SBUs readily accommodate structural defects, such as missing clusters or linkers [12], and post-synthetic metal insertions [13]. In addition, the widely encountered $Zr_6(\mu_3\text{-}O)_4(\mu_3\text{-}OH)_4$ node supports a broad range of connectivities, typically from 4- to 12-connected

architectures [14], with a few reported exceptions reaching even higher coordination numbers [15].

Following the development of UiO-66 [16], more complex Zr-based topologies such as NU-1000 were subsequently introduced [17]. In NU-1000, Zr nodes are coordinated by tetratopic pyrene-based linkers to generate a framework with large mesoporous channels and photoactive organic components. These structural features make NU-1000 particularly attractive for the integration of optical functionality within a robust porous architecture [18, 19].

On the other hand, plasmonic nanoparticles (NPs) exhibit distinctive optical properties arising from localized surface plasmon resonance (LSPR), that is, the collective oscillation of conduction electrons under light irradiation [20]. The position and intensity of the LSPR depend on the dielectric environment, metal composition, particle size, surface chemistry, and, particularly, particle shape [21–23]. In anisotropic nanoparticles, shape-dependent plasmon modes can extend the optical response from the visible into the near-infrared region (NIR), which is especially relevant for photothermal and sensing applications.

The sensitivity of the LSPR to the local dielectric environment has made plasmonic NPs valuable platforms for optical sensing [24, 25]. In addition, plasmon excitation can drive efficient non-radiative relaxation and heat generation [26], while the associated local field enhancement can amplify Raman scattering from nearby molecules, enabling surface-enhanced Raman scattering (SERS) [27–29]. These properties make plasmonic nanostructures particularly attractive for multifunctional optical applications.

Therefore, integrating plasmonic nanoparticles with MOFs into hybrid nanocomposites is an attractive strategy to combine porosity with advanced optical functionality. However, this remains challenging because the conditions required for MOF crystallization can compromise the morphology and optical response of preformed plasmonic nanoparticles [30–32]. Two main synthetic approaches have been explored to address this issue: impregnation of a preformed MOF with a metal precursor followed by reduction, which typically yields small metallic domains with limited control over size and distribution, and core-shell growth, in which the MOF is formed around pre-synthesized plasmonic seeds [33]. The latter strategy is particularly appealing, although it requires careful control over the synthesis conditions to preserve the properties of the plasmonic core.

In this work, we present a seed-mediated strategy for the synthesis of AuNP@NU-1000 nanocomposites. While plasmonic composites based on frameworks such as ZIF-8 are well documented [34–38], stable combinations of anisotropic plasmonic nanoparticles with Zr-based MOFs remain comparatively scarce [39, 40]. We examine how nanoparticle shape and concentration affect the optical response of the resulting core-shell materials, including photoluminescence quenching, photothermal heating, and SERS performance in colloidal dispersion. Finally, using wide-field hyperspectral microscopy, we map the independent optical signatures of the plasmonic core and MOF shell after cellular internalization, providing label-free intracellular optical readout of the nanocomposites.

2 | Results and Discussion

2.1 | Synthesis and Structural Characterization of NU-1000 nanoMOFs and Nanocomposites

Most Zr-based MOFs require elevated temperatures and prolonged reaction times to achieve proper crystallization because of the strong coordination between the metal nodes and organic linkers. This constraint applies regardless of whether the final material is isolated as nanoparticles, microcrystals, or single crystals. In contrast, NU-1000 can be obtained under comparatively mild conditions, requiring only 90°C and approximately 30 min [41]. Other frameworks, such as the UiO series [16], generally need harsher synthesis conditions [42]. This relative synthetic accessibility makes NU-1000 an attractive platform for the preparation of plasmonic nanoMOF composites.

Figure 1a illustrates the synthesis of NU-1000 nanocomposites from $ZrOCl_2 \cdot 8H_2O$ and H_4TBAPy in a DMF/water medium using acetic acid as a modulator and PEGylated AuBipy as seeds (see Experimental Section for details). The resulting MOF adopts a hexagonal structure with interconnected triangular and hexagonal channels (Figure S1). Field emission scanning electron microscopy (FE-SEM) images of pristine NU-1000 nanoMOFs (Figure S2) show a rice-like morphology. The particles are polydisperse, with an average length of 378 ± 76 nm and width of 145 ± 25 nm, as determined from the size distributions shown in Figure S3.

The incorporation of PEGylated plasmonic nanoparticles during NU-1000 synthesis led to the formation of plasmonic nanoMOFs. Two nanoparticle types were employed: AuBipy (Figure S4), with an average length of 77 ± 4 nm and width of 28 ± 3 nm, and gold nanorods (AuNRs), with an average length of 41 ± 3 nm and width of 10 ± 1 nm (Figure S5). Some Au nanosphere impurities can be observed due to the formation of single-crystalline nanospheres during the aging process used to produce pentatwinned seeds; however, their absorbance does not contribute to the longitudinal LSPR band [43]. As noted above, NU-1000 crystallization requires heating at 90°C to enable formation of the $Zr_6(\mu_3\text{-}O)_4(\mu_3\text{-}OH)_4$ SBU from the Zr precursor. Because temperature can alter nanoparticle morphology, this effect was examined carefully, as such changes directly affect key physicochemical properties including LSPR absorption and heat generation.

Figure 1b–d shows high-resolution transmission electron microscopy (HR-TEM) images of core-shell nanocomposites consisting of PEGylated AuBipy cores prepared at seed concentrations of 2 nM, 5 nM, and 10 nM, respectively, coated with a NU-1000 shell. The crystalline nature of the shell was confirmed by fast Fourier transform (FFT) analysis, which revealed interplanar distances corresponding to the (100), (200), and (300) crystallographic planes (Figure 1e). Complementary FE-SEM analysis of these nanocomposites is shown in Figure S6. Nanocomposites prepared with PEGylated AuNRs at 10 nM, 20 nM, and 50 nMM were likewise characterized by TEM (Figure S7) and FE-SEM (Figure S8). The different concentration ranges used for AuBipy and AuNRs reflect the effect of seed size on nanocomposite growth, with larger nanoparticles requiring lower seed concentrations than smaller ones. FE-SEM images acquired

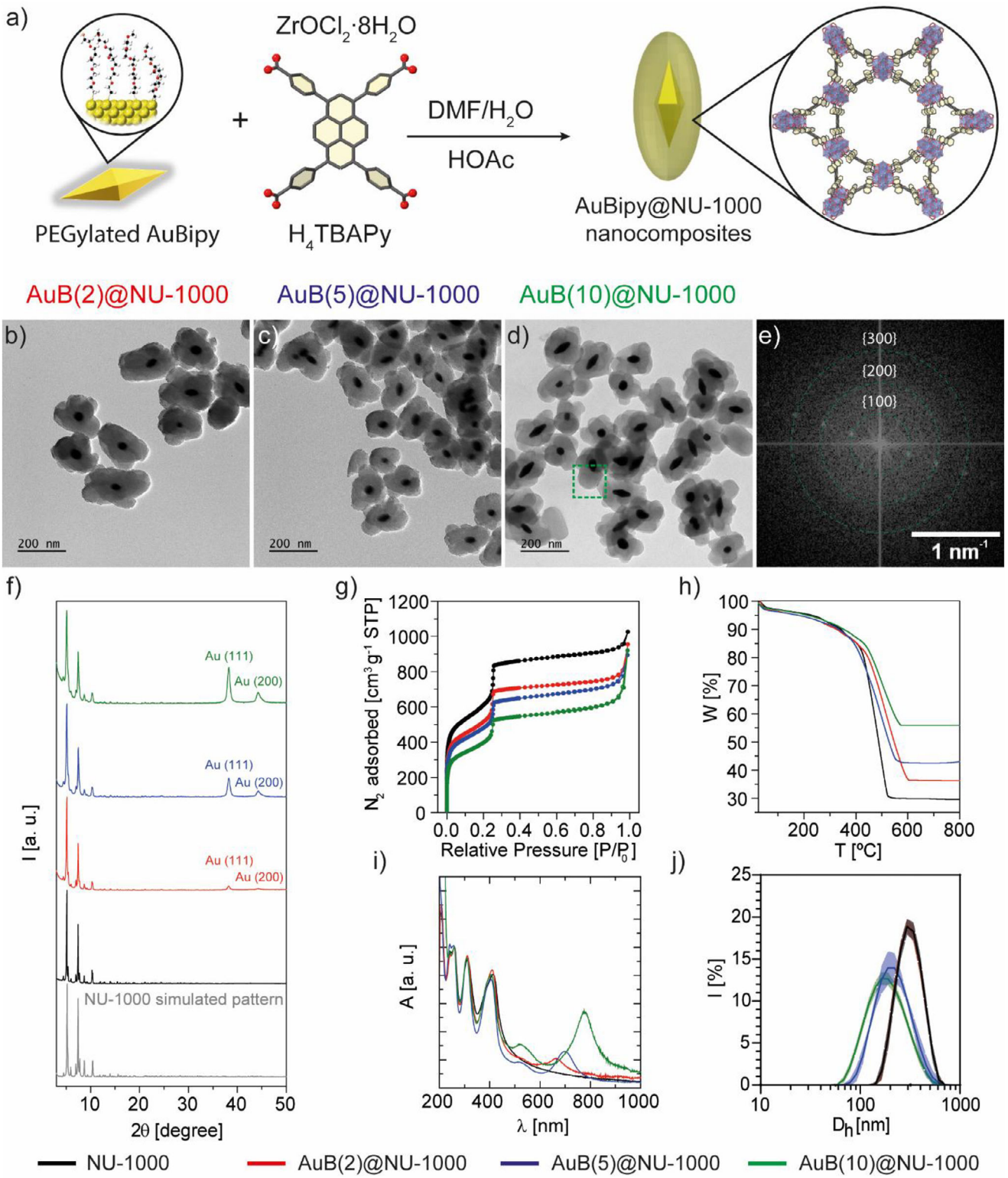

FIGURE 1 | (a) Synthetic scheme of AuBipy@NU-1000 nanocomposites using PEGylated AuBipy as the core. HR-TEM images of (b) AuB(2)@NU-1000, (c) AuB(5)@NU-1000, and (d) AuB(10)@NU-1000 nanocomposites, with (e) FFT highlighting the crystallographic planes of AuB(10)@NU-1000. f) PXRD patterns. (g) N_2 adsorption isotherms at 77 K. (h) TGA thermograms. (i) UVvis spectra. (j) DLS analysis of NU-1000 and its PEGylated AuBipy nanocomposites.

with secondary- and backscattered-electron detectors (Figures S6 and S8) provide complementary structural information, revealing the external morphology of the nanocomposites and the presence of the Au cores, respectively. In all cases, the nanocomposites are smaller than pristine NU-1000 (Figures S2 and S3), consistent with a seeded-growth mechanism in which shell thickness decreases as seed concentration increases [40].

Statistical analysis based on an average of 135 particles per sample (82–164 particles) confirms the effectiveness of the seeded-growth strategy (Table S1). For the Au bipyramid series, increasing the seed concentration from AuB(2) to AuB(10) raises the fraction of particles containing an encapsulated Au core from 77.2% to 97.2%, while the percentage of empty NU-1000 particles decreases from 22.8% to 2.8%. A similar trend is observed for the Au nanorod series, where the encapsulation efficiency increases from 66.4% for AuR(10) to 94.7% for AuR(50), corresponding to a reduction in empty particles from 33.6% to 5.3%. These results demonstrate that increasing the seed concentration substantially improves the probability of heterogeneous MOF growth on the Au nanoparticle surface while suppressing the formation of core-free NU-1000 particles.

The powder X-ray diffraction (PXRD) patterns of both nanocomposite series match the simulated diffraction profile of NU-1000 in a hexagonal lattice (Figure 1f; Figure S9a). With increasing nanoparticle concentration, the intensities of the first two Au reflections at 38.2° and 44.4° (2θ), assigned to the (111) and (200) planes, respectively, become more pronounced. Pawley refinement of pristine NU-1000 (Figure S10) confirms a crystal structure in the P6/mmm space group with unit cell parameters of a = b = 39.5486 Å and c = 16.3391 Å, consistent with the FFT analysis in Figure 1e and excluding the presence of the NU-901 polymorph [44].

N_2 adsorption isotherms at 77 K (Figure 1g; Figure S9b) show reduced uptake for the nanocomposites relative to pristine NU-1000, consistent with the presence of a nonporous and much denser Au component. Brunauer-Emmett-Teller (BET) surface areas were calculated using BETSI analysis (Figures S11–S17) [45]. To account for the porous fraction of the nanocomposites, the Au content was estimated from thermogravimetric analysis (TGA) by subtracting the inorganic residue of pristine NU-1000, assigned to the inorganic residue (ZrO_2), from that of the composites (Table S2). TGA also confirmed thermal stability up to 400°C for both pristine NU-1000 and the nanocomposites (Figure 1h; Figure S9c). The pore size distributions of NU-1000 and its nanocomposites were analyzed using a non-local density functional theory (NLDFT) model for cylindrical pores (Figure S18a,b), revealing three pore sizes associated with the intrinsic cavities of NU-1000: a micropore of approximately 11.9 Å and two mesopores of 23.6 Å and 31.3 Å (Figure S18c).

The UV-vis spectra in Figure 1i and Figure S9d show the absorption profiles of both nanocomposite series. The bands at 250 nm, 320 nm, and 410 nm are assigned to π–π transitions of the H_4TBAPy linker [46]. In the NIR region, the LSPR bands of AuBipy and AuNRs are preserved, although both series exhibit a blue shift at lower nanoparticle concentrations. This trend is partly related to differences in MOF shell thickness. However, the much larger shift observed for the AuBipy series indicates that shell thickness alone cannot account for the optical response. Instead, the data point to partial reshaping of the plasmonic cores under the NU-1000 synthesis conditions (90°C, 30 min).

To examine this effect in more detail, high-magnification FE-SEM images were acquired using both secondary- and backscattered-electron detectors (Figure S19). At the lowest PEGylated AuBipy concentration (2 nM), pronounced reshaping was observed, with bipyramidal particles evolving toward avoid morphologies and a corresponding LSPR shift from 800 nm to 650 nm. At 5 nM, the particles displayed blunted tips, consistent with an intermediate shift to 700 nm. In contrast, at the highest concentration (10 nM), the bipyramidal morphology was largely preserved. These results indicate that seed concentration affects not only the shell thickness during nanocomposite growth, but also the extent of reshaping of the plasmonic core.

To further support this interpretation, 3D electron tomography with in situ heating at 90°C was performed [47, 48]. Under these conditions, the AuBipy cores undergo gradual structural deformation, with subtle but detectable changes in nanoparticle morphology. Video S1 shows tomographic reconstructions of the same AuBipy particle at different time points, where regions of volume loss (red) and gain (blue) illustrate the reshaping process, even under vacuum. For comparison, the highly seeded AuB(10)@NU-1000 nanocomposite was subjected to the same in situ heating treatment. In this case, no redistribution of the gold core mass was observed (Video S2), whereas only minor changes were detected in the MOF shell (Videos S3 and S4). These observations support the view that the MOF shell helps preserve the morphology of the plasmonic core under the synthesis conditions.

Dynamic light scattering (DLS) measurements further support a seeded-growth mechanism across the different particle concentrations (Figure 1j; Figure S9e). For both nanoparticle series, the hydrodynamic size decreases as seed concentration increases (Table S3), which is in agreement with the UV-vis spectra shown in Figure 1i and Figure S9d; increasing the shell thickness results in a larger change in the dielectric environment, leading to a more pronounced blue shift of the characteristic LSPR absorption band. In addition, the polydispersity index (PdI) decreases to values below 0.2 relative to pristine NU-1000, indicating improved colloidal uniformity in the nanocomposite samples.

2.2 | Effect of Shell Thickness and Particle Shape on Photoluminescence Properties

We next evaluated the influence of nanoparticle shape and concentration on the photoluminescence of NU-1000 (Figure 2). Pristine NU-1000 displays an emission spectrum centered at 450 nm, comprising a shorter-wavelength band assigned to $S_1 \rightarrow S_0$ transitions and a longer-wavelength contribution attributed to excimer emission [49, 50]. Incorporation of plasmonic cores leads to pronounced photoluminescence quenching, consistent with previous observations in related MOF-based plasmonic systems [40]. This attenuation is consistent with non-radiative energy-transfer processes such as Förster resonance energy transfer (FRET) and nanometal surface energy transfer (NSET) [51, 52]. The non-radiative relaxation of the photoexcited pyrene linker

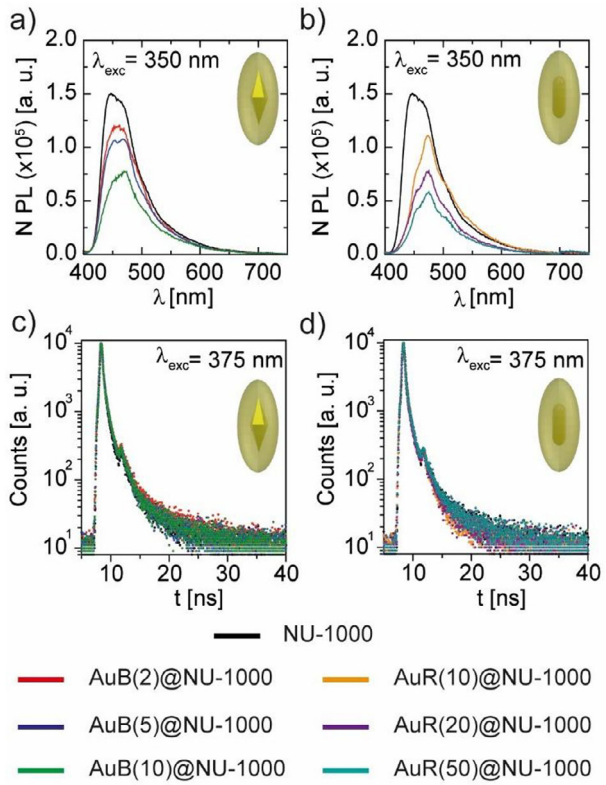

FIGURE 2 | Emission spectra of (a) AuBipy@NU-1000 and (b) AuNRs@NU-1000 under 350 nm excitation, and time-correlated single photon counting decay kinetics (375 nm excitation) of (c) and (d), respectively.

toward the gold core can be described within the framework of through-space energy transfer, which requires spectral overlap between donor emission and acceptor absorption together with nanometric donor-acceptor separation, conditions met here by the linker emission and the broad plasmonic absorption of the core across the shell thickness. We note, and now state explicitly, that for a metallic nanoparticle acceptor the appropriate description is NSET together with plasmon-mediated quenching, with classical point-dipole FRET representing a limiting contribution rather than the dominant channel.

The extent of photoluminescence quenching for each sample is summarized in Table S4 and increases with the gold content determined by ICP-OES (Figure S20). This trend is also consistent with the increasingly dominant optical contribution of the metallic component at higher seed concentrations (Figure S20). Notably, the quenching behavior depends on core geometry. In the AuBipy series (Figure 2a), both the $S_1 \rightarrow S_0$ and excimer contributions decrease progressively. In contrast, the AuNRs series (Figure 2b) shows a much stronger suppression of the $S_1 \rightarrow S_0$ contribution, while the excimer band decreases more gradually with increasing gold concentration. This quenching efficiencies are attributed to two main factors: (i) the different spectral overlap between the NU-1000 linker emission and the absorption of each plasmonic core (Figures S4a and S5a), which modulates the efficiency of non-radiative energy transfer, and (ii) the different local-field distribution and gold content per particle of bipyramids versus rods (ICP-OES, Figure S20), which set the magnitude of plasmon-mediated quenching. The sharper tips and field localization of AuBipy versus the elongated geometry of AuNRs lead to distinct coupling to the two emissive populations of the linker.

Time-correlated single-photon counting (TCSPC) analysis of both nanocomposite series revealed no significant changes in emission lifetime relative to pristine NU-1000 (Figure 2c,d). The pristine framework exhibits an average lifetime of 0.40 ns (Table S5), obtained from multiexponential fitting using Equation S1. Despite the pronounced decrease in steady-state emission intensity, the average excited-state lifetime remains essentially unchanged (≈0.40 ns) for both nanocomposite series. This decoupling of emission intensity from excited-state lifetime is the established hallmark of a predominantly static quenching mechanism, as a dynamic (collisional or energy-transfer) process would be expected to shorten the measured lifetime in proportion to the decrease in emission intensity. The absence of such lifetime shortening therefore supports the assignment of predominantly static quenching. In this scenario, only the emissive fraction of the linker population contributes to the detected signal, while coupling to the plasmonic cores reduces the overall emission intensity without strongly affecting the measured lifetime [53].

2.3 | Heating of AuNPs@NU-1000 Nanocomposites Properties Under Near Infrared Radiation

We evaluated the macroscopic heating performance of the nanocomposites by recording temperature-time profiles under 808 nm laser irradiation (Figure 3). Nanocomposites containing AuNRs (50 nM) or AuBipy (10 nM) cores were functionalized with MeO-PEG-PO_3 following established protocols [40, 54]. This surface modification was confirmed by the inversion of the ζ-potential from positive to negative values (Figure S21), consistent with the presence of deprotonated phosphate groups and improved colloidal stability during optical excitation. The samples were then exposed to a continuous-wave 808 nm laser. As described above, both nanocomposite types exhibit LSPR absorption near this wavelength (Figure 1i; Figure S9d), enabling efficient photothermal conversion. Although the NU-1000 shell is poorly conductive, the heat generated in the metallic core is transferred efficiently to the surrounding aqueous medium, and the resulting temperature evolution was monitored continuously (Figure 3a).

Nanoparticle tracking analysis (NTA) was used to quantify the concentration of the dispersions evaluated, namely PEGylated NU-1000, AuB(10)@NU-1000, and AuR(50)@NU-1000 (Figure S22 and Table S6) in order to normalize the heating-cooling curves on a per-nanocomposite-particle basis. For the heating experiments, 200 μL of a 200 pM nanosystem dispersion was irradiated. Different irradiances (10 W cm^{-2}, 5 W cm^{-2}, and 2.5 W cm^{-2}) were tested at constant nanocomposite concentration. It should be emphasized that these high-irradiance conditions, which lead to temperatures approaching the boiling point of the solvent, were deliberately selected as a stringent test of the plasmonic stability and photothermal performance of the nanocomposites. These experimental conditions are intended to evaluate the robustness of the materials under extreme operating

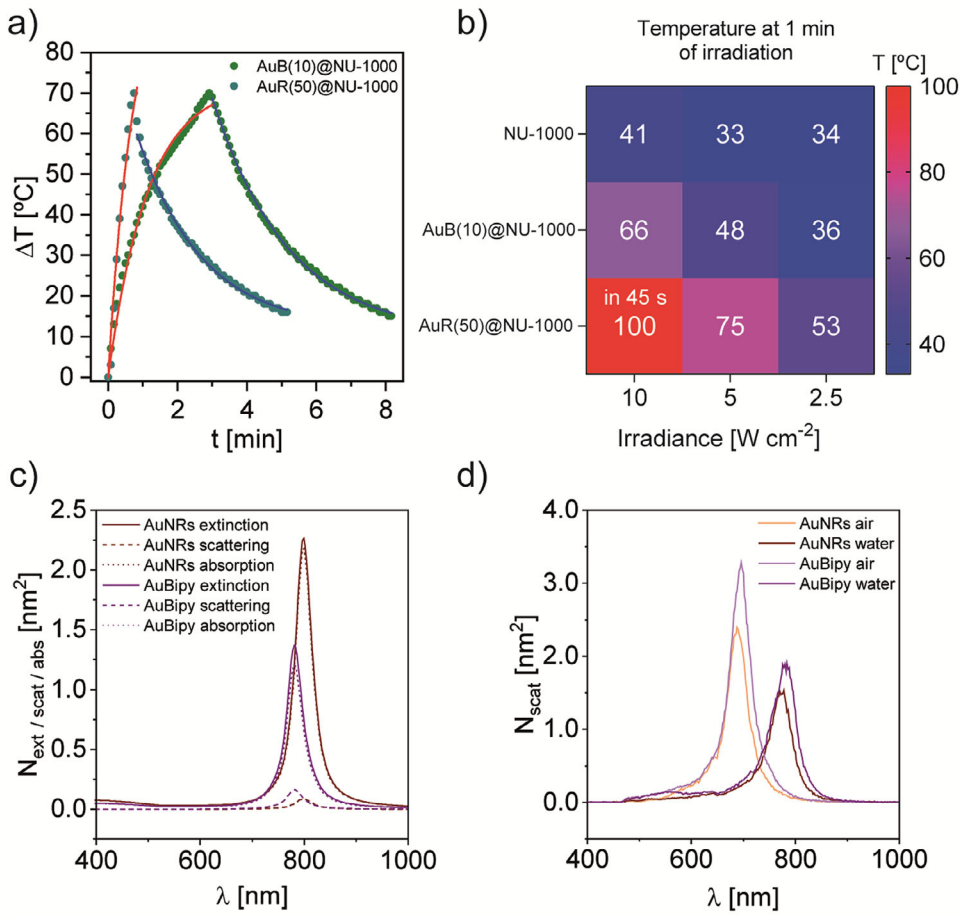

FIGURE 3 | (a) Heating-cooling curves of AuB(10)@NU-1000 and AuR(50)@NU-1000 nanocomposites under 808 nm laser irradiation at an irradiance of 10 W cm^{-2}, recorded until reaching the boiling point of water ($\Delta T = 70°C$). (b) Heating map summarizing the maximum temperature reached by NU-1000 nanoparticles and their corresponding nanocomposites at different irradiances after 1 min of irradiation. (c) Simulated extinction, scattering, and absorption spectra of AuBipy and AuNRs, normalized to the volume of each particle. (d) Scattering spectra of a single nanoparticle of AuNR and AuBipy on the glass in air and water atmosphere.

conditions and are not representative of the significantly lower irradiation intensities employed in cell-treatment experiments. Under these conditions, the AuNRs-based nanocomposites produced temperature increases of more than 50°C within 1 min, even at irradiances as low as 2.5 or 5 W cm^{-2} (Figure 3b). In Figure 3a and Figure S23, the red curves correspond to the heating profiles fitted with the Box-Lucas function, whereas the blue curves represent the cooling profiles fitted with an exponential decay model (Table S7).

The heating-cooling profiles show that the AuNRs-based nanocomposites reach the boiling point of water faster than their AuBipy counterparts (Figure 3a). This occurs despite the AuBipy system containing nearly twice as much gold per mass of nanocomposite according to ICP-OES (Figure S20b), and approximately five times more gold per particle volume (Figure S24). The faster heating of the AuNRs-based composites can be rationalized from the simulated extinction, scattering, and absorption spectra of both plasmonic cores [20]. When normalized by particle volume (Figure 3c; Figure S24), three differences become apparent: (i) the LSPR of AuNRs is closer to resonance with the 808 nm excitation source, with a maximum absorption near 800 nm, whereas AuBipy peaks at 782 nm; (ii) AuNRs exhibit a higher absorption cross-section per unit volume; and (iii) their elongated geometry leads to substantially lower scattering than AuBipy. As a result, a larger fraction of the incident energy is absorbed and dissipated as heat rather than scattered, giving rise to a more efficient photothermal response in the AuNRs-based nanocomposites.

To further examine the origin of the enhanced photothermal response, single-particle dark-field scattering spectra were measured for individual AuBipy and AuNRs nanoparticles in air and water (Figure 3d; Figures S25–S27). In air, the dominant scattering peak of AuBipy is centered at $\lambda = 692$ nm, whereas AuNRs show their main peak at $\lambda = 690$ nm. Upon water immersion, both particle types exhibit a pronounced red shift, consistent with the higher refractive index of the surrounding medium. The experimentally observed peak positions in air do not fully coincide with the simulated spectra, which is attributed to the presence of a CTAB ligand shell that increases the effective local refractive index and induces an additional red shift relative to a bare metal-air interface [55, 56]. AuBipy nanoparticles also exhibit higher scattering intensities than AuNRs, although the absolute intensity depends strongly on particle orientation with respect to the incident polarization [57–59]. These single-particle

observations are consistent with both the simulated spectra and the faster heating of the AuNRs-based nanocomposites, supporting the conclusion that reduced scattering losses and more efficient absorption, rather than total gold content alone, underlie their superior photothermal performance.

Beyond the heating-cooling profiles, both nanocomposite systems retained their heating performance over multiple irradiation cycles under identical excitation conditions. Upon 808 nm irradiation, the boiling point of water was reached for at least three consecutive cycles (Figure S28). These results indicate that the MOF shell not only preserves the structural integrity of the plasmonic core under thermal stress but also allows repeated photothermal actuation without an evident loss of performance. Consistent with this interpretation, 3D electron tomography showed that the AuBipy core remains well confined within the AuB(10)@NU-1000 nanocomposite after heating at 90°C for 3 h (Videos S2–S4), in contrast to the mass redistribution observed for bare AuBipy under similar conditions (Video S1). A similar stabilizing effect of MOF shells on plasmonic cores has been reported previously by our group using related systems [40]. Furthermore, the spatial distribution of the Au core within the NU-1000 shell is supported by the combined evidence provided by FE-SEM with a backscattered electron detector, HR-TEM, and 3D electron tomography.

2.4 | AuBipy@NU-1000 Nanocomposites as SERS Substrate in Colloidal Dispersion

As proof of concept, the AuB(10)@NU-1000 nanocomposite was evaluated as a SERS-active colloidal substrate. This formulation was selected for two reasons. First, the sharp tips of AuBipy generate intrinsic hot spots without requiring particle-particle coupling [60]. Second, its LSPR is centered at 775 nm, slightly blue-shifted relative to the 785 nm Raman excitation wavelength (Figure 1i). This spectral arrangement is favorable for colloidal SERS measurements, as previously reported for anisotropic gold nanostructures under off-resonance conditions [61]. This behavior differs from SERS studies performed on molecules adsorbed onto roughened or nanostructured metallic surfaces, where the maximum enhancement typically occurs at or red-shifted from the excitation wavelength. Such differences are attributed to the interplay between enhancement and optical extinction at both the excitation and scattered wavelengths.

The Raman reporter molecule employed for the AuB(10)@NU-1000 nanocomposite was 4-mercaptobenzonitrile (4-MBN) (Figure S29). 4-MBN was selected because its thiol group enables covalent anchoring to the gold surface, whereas its nitrile functionality gives rise to a distinct Raman band at 2232 cm^{-1} in the "cellular silent region", thereby minimizing overlap with common organic vibrations [58]. The principal Raman bands of 4-MBN detected using AuB(10)@NU-1000 as a colloidal SERS substrate are summarized in Table S8 [62].

The PEG chains grafted onto the AuBipy surface are not expected to contribute significantly to the Raman response because of their low polarizability. 4-MBN solutions in methanol, with concentrations ranging from 5 μM to 500 pM, were incubated overnight with the as-synthesized AuB(10)@NU-1000 dispersion (200 μL, approximately 1×10^{12} particles mL^{-1}) to allow diffusion through the MOF porosity and covalent attachment to the AuBipy surface. Figure 4a compares the Raman spectrum of pristine NU-1000 and AuB(10)@NU-1000, with those obtained after exposure to 4-MBN solutions, enabling the assignment of the 4-MBN vibrational bands, while metallic gold does not possess Raman-active vibrational modes and therefore does not exhibit intrinsic Raman bands. Under these conditions, a detection limit of 5 nM was established for this nanocomposite, corresponding to the concentration at which the background-subtracted nitrile band at 2232 cm^{-1} is detected with a signal-to-noise ratio (S/N) ≥ 3, as determined relative to the baseline noise of the pristine substrate spectrum.

To further assess the sensitivity of the system, serial dilutions of the previously tested colloidal suspension (10-, 25-, 50-, 75-, and 100-fold) were prepared, and the same incubation protocol was applied using proportionally diluted analyte solutions. Figure 4b–e shows the intensities of the four characteristic Raman bands of 4-MBN (Table S8) as a function of analyte concentration and nanocomposite dilution (Figure S30). Notably, all four vibrational modes remained detectable after a 50-fold dilution of the original colloid (1×10^{12} particles mL^{-1}). At the highest analyte concentration tested (5 μM), the Raman signal was still observable even at 75- and 100-fold nanocomposite dilution. It should be noted that the analyte concentration is given in solution, whereas adsorption within the MOF can reduce the free analyte fraction, so that only a portion of the molecules is expected to reach the vicinity of the plasmonic core where the SERS enhancement occurs.

2.5 | Hyperspectral Microscopy of Intracellular AuB(10)@NU-1000 Nanocomposites

Before evaluating the intracellular optical response of the nanocomposites, their effect on cell viability was assessed in A549 cells using an MTT assay (Figure S31). After 6 h of incubation, both PEGylated and non-PEGylated AuB(10)@NU-1000 formulations maintained high cellular viability across the concentration range tested, up to 200 pM. Based on these results, and after dose normalization by ICP-OES, a concentration of 100 pM was selected for the subsequent imaging experiments. This dose corresponds to 6×10^{10} particles·mL^{-1}, containing 15.0 μg·mL^{-1} of Au and 13.8 μg·mL^{-1} of Zr. Under these conditions, the 6 h incubation provided a practical balance between preserving cell viability and obtaining a sufficiently strong optical signal for hyperspectral analysis.

To investigate the intracellular distribution of the nanocomposites, we employed wide-field hyperspectral microscopy using the IMA system (Photon Etc., Montreal). This platform collects spectral information over a broad Vis-NIR range (400 nm to 900 nm) in a label-free manner, enabling simultaneous optical readout of both the plasmonic and MOF components. Cellular boundaries and basal anatomy were defined from the intrinsic optical scattering of the biological matrix by averaging the 590-610 nm spectral window (Figure 5a). The full hyperspectral unmixing workflow for both PEGylated and non-PEGylated formulations is provided in Figures S32 and S33, respectively.

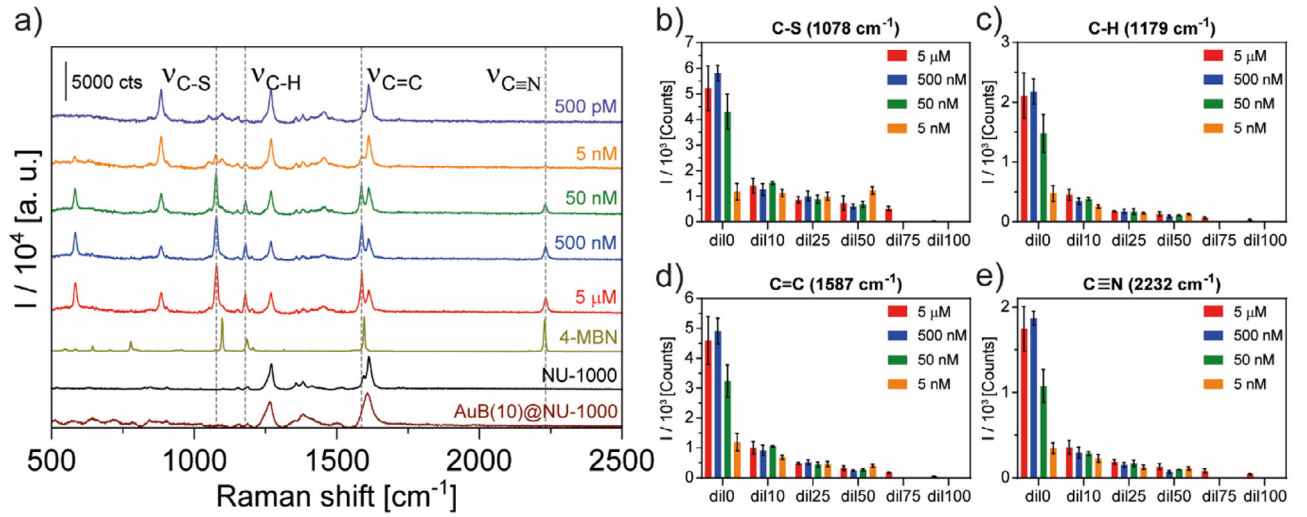

FIGURE 4 | (a) Raman spectra of MBN at different concentrations using AuB(10)@NU-1000 colloidal suspensions (1×10^{12} particles mL^{-1}). Corresponding Raman intensities of 4-MBN at various dilutions, obtained using different dilutions of the colloidal SERS substrate, for the (b) C—S, (c) C—H, (d) C═C, and (e) C≡N vibration modes.

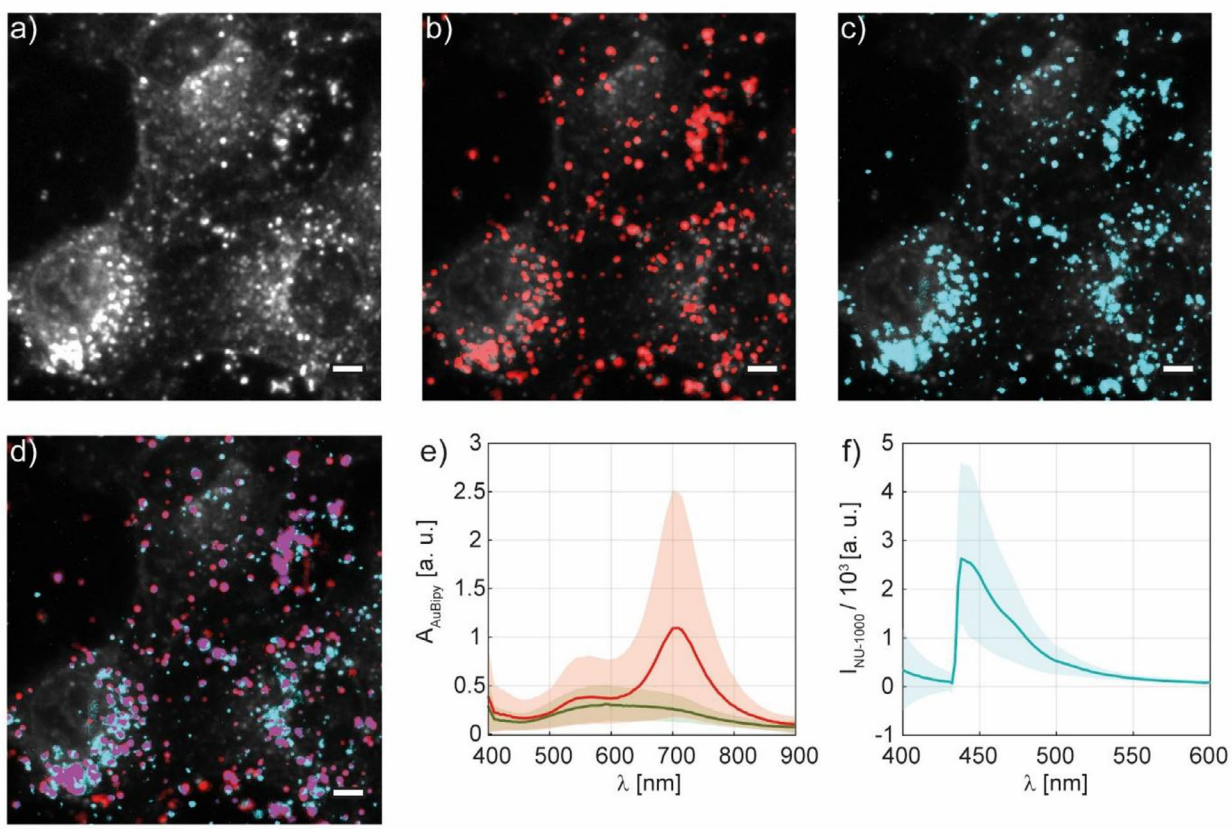

FIGURE 5 | Hyperspectral optical readout of intracellular PEGylated AuBipy@NU-1000 nanocomposites. (a) Optical scattering map integrated over the 590-610 nm spectral range, showing the morphology of A549 cells incubated with the nanocomposite. (b) Spatial distribution of the plasmonic AuBipy core, mapped in false-color red through its differential NIR absorbance signal and overlaid on the scattering map. (c) Intracellular localization of the NU-1000 shell, represented in cyan based on its intrinsic fluorescence emission under ultraviolet excitation. (d) Merged colocalization map showing the spatial overlap of both optical components inside cells. The spatial panels shown here correspond to an approximately 4× magnified region of interest extracted from the full field of view presented in Figure S32. Scale bars in all spatial images represent 20 μm. (e) Mean extracted optical absorbance spectra, where the green line corresponds to the basal cellular scattering background and the red line shows the longitudinal surface plasmon resonance band of AuBipy around 720 nm. (f) Mean fluorescence spectrum showing the characteristic emission band of the NU-1000 shell at 438 nm. In both spectral panels, the shaded regions represent the 10^{th}-90^{th} percentile distribution of the validated pixels.

The spatial distribution of the plasmonic AuBipy core was mapped through its differential near-infrared absorbance signal (Figure 5b). Detection was based on a simple spectral criterion in which the mean near-infrared absorbance (650-900 nm) exceeded the visible scattering reference, thereby minimizing the contribution from the basal cellular background. In parallel, because the main absorption bands of the pyrene-based linker lie largely outside the effective detection window of the hyperspectral setup, the NU-1000 shell was tracked through its characteristic fluorescence emission centred at 438 nm (Figure 5c), using a threshold defined as three standard deviations above the mean autofluorescence of untreated control cells.

The merged colocalization maps show a substantial spatial overlap between both optical components inside cells (Figure 5d). In addition, the extracted intracellular spectra retained the characteristic longitudinal plasmon resonance of AuBipy (Figure 5e) and the emission band of the NU-1000 shell (Figure 5f), supporting preservation of the coupled optical identity of the nanocomposite after internalization.

Spatial colocalization analysis between the plasmonic absorbance and MOF fluorescence signals in the PEGylated samples yielded a high global Pearson correlation coefficient ($R = 0.77 \pm 0.07$, $n = 6$). These data support retention of the associated core-shell optical signatures after endocytic uptake. In contrast, the non-PEGylated formulations showed evident colloidal instability in culture medium, forming extracellular aggregates that adhered strongly to the glass substrate and cell membrane despite repeated washing (Figure S33). Although these aggregated samples still exhibited significant spatial colocalization ($R = 0.69 \pm 0.04$, $n = 4$), the lower correlation coefficient ($p = 0.0497$) is consistent with the visual evidence of aggregation. The presence of large 3D aggregates also introduces spatio-spectral artifacts during sequential hyperspectral acquisition, including apparent mismatch between the near-infrared absorbance and fluorescence signals and out-of-focus optical halos that complicate the unmixing process.

The physical relevance of these spatial correlations was further supported by the corresponding spatial correlograms (Figures S32k and S33k), which showed maximum correlation values at zero-pixel shift for both colloidal states. Altogether, these results identify PEGylated AuB(10)@NU-1000 nanocomposites as robust intracellular optical probes and support the preservation of their coupled core–shell signatures after cellular internalization.

3 | Conclusion

In summary, we have developed plasmonic core-shell nanocomposites based on gold nanoparticles encapsulated within NU-1000 nanoMOFs through a seed-mediated growth strategy. This approach enables the integration of plasmonic and porous functionalities within a single nanostructure while preserving the optical response of the metallic cores under MOF synthesis conditions.

The resulting nanocomposites exhibit tunable optical behavior governed by nanoparticle shape and concentration, including photoluminescence quenching, efficient photothermal heating under near-infrared irradiation, and SERS activity in colloidal dispersion. Notably, nanorod-based systems show a stronger photothermal response, which is consistent with their more favorable balance between absorption and scattering.

Importantly, wide-field hyperspectral microscopy enables label-free intracellular readout of the plasmonic core and MOF shell by independently tracking the optical signatures of both components after cellular internalization. The substantial spatial correlation between these signals supports preservation of the coupled core-shell optical identity of the nanocomposites inside cells.

Overall, these results establish plasmonic NU-1000 nanocomposites as robust intracellular optical probes and highlight the potential of combining plasmonic cores with photoactive MOF shells in multifunctional hybrid nanomaterials.

4 | Experimental Section

4.1 | Chemicals

Zirconyl chloride octahydrate ($ZrOCl_2 \cdot 8H_2O$, 98%), silver nitrate ($AgNO_3$, ≥99.0%); L-Ascorbic acid ($C_6H_8O_6$, ≥99%); sodium borohydride ($NaBH_4$, ≥98.0%); citric acid (≥99.5%); cetyltrimethylammonium chloride (CTAC, 25 wt% in H_2O); hexadecyltrimethylammonium bromide (CTAB, ≥98%); poly(ethylene glycol) methyl ether thiol (MeO-PEG-SH, 2 kDa) were provided by Sigma-Aldrich. Glacial acetic acid (CH_3COOH, 99.7%); DMF (≥99.8%); hydrogen tetrachloroaurate (III) hydrate ($HAuCl_4$, Au≥49%) were provided by Thermo Scientific, and H_4TBAPy ($C_{44}H_{26}O_8$, 97%) was provided by Alfa Chemical. Hydrochloric acid (HCl, 37%); N,N-dimethylformamide (DMF, ≥99.8%); chloroform ($CHCl_3$, ≥99.8%) were provided by Fisher Scientific.

4.2 | General Considerations

All glassware was washed with reagent and rinsed with Milli-Q water, then followed by aqua regia prior to use and rinsed carefully with Milli-Q water and acetone.

4.3 | Synthesis of AuNRs

4.3.1 | Synthesis of Seeds

A 0.2 M stock solution of cetyltrimethylammonium bromide (CTAB) was prepared and preheated to 40°C before each reaction to ensure complete dissolution and optical clarity. An aqueous solution of $HAuCl_4$ (0.25 mL, 0.01 M) was then added to 7.5 mL of the 0.2 M CTAB solution, and the mixture was equilibrated in a water bath maintained at 26°C. Subsequently, a freshly prepared $NaBH_4$ solution (600 µL, 0.01M) was rapidly injected into the vigorously stirred solution (350 rpm), and stirring continued for 2 min. To ensure complete decomposition of residual $NaBH_4$, the resulting seed solution was aged for 1 h at room temperature prior to use in the growth step.

The resulting seed solution typically exhibits a clear yellow-brown color. If the solution appears excessively dark, the forma-

tion of gold nanorods (AuNRs) may be inhibited, favoring the generation of spherical gold nanoparticles [63].

4.3.2 | Seed-Mediated Growth Synthesis of Au Nanorods (AuNRs)

A 0.2 Mm solution of cetyltrimethylammonium bromide (CTAB, 100 mL) was transferred to a 250 mL glass vessel and equilibrated at 26°C. An aqueous solution of $HAuCl_4$ (0.01 M, 4.25 mL) was then added, and the mixture was stirred at 350 rpm until thermal equilibration was achieved. Subsequently, a solution of $AgNO_3$ (0.01 M, 1.23 mL) was introduced, followed by stirring for 2 min. A freshly prepared ascorbic acid solution (0.1 M, 680 µL) was then added, and the mixture was stirred for an additional 10 min. Finally, 1.1 mL of the pre-prepared seed solution, maintained at 26°C to prevent CTAB crystallization, was injected, and stirring was continued for a further 2 min. The reaction mixture was then left undisturbed overnight in a water bath at 26°C [43].

The resulting product was collected by centrifugation at 10,000 rcf for 30 min at 28°C, a step that was carried out as rapidly as possible to avoid CTAB crystallization. The sample was washed twice with water under the same conditions and finally redispersed in an aqueous CTAB solution (0.16 mg mL^{-1}).

4.4 | Synthesis of AuBipy

4.4.1 | Synthesis of Pentatwinned Seeds

Initial gold seed nanoparticles were prepared in a 20 mL glass vial by mixing 8.639 mL of water, 0.661 mL of a CTAB solution, and 0.100 mL of an aqueous $HAuCl_4$ solution (25 mM) under vigorous magnetic stirring (1,000 rpm) for 5 min. Subsequently, 0.100 mL of an aqueous citric acid solution (0.5 M) was added to the reaction mixture, immediately followed by the successive, continuous addition of two aliquots (0.25 mL each) of freshly prepared $NaBH_4$ solution (25 mM, aqueous). The solution color changed from pale yellow to brown, indicating the formation of gold seeds. After 2 min of stirring, the vial was sealed, and the seed solution was aged in a heating block at 80°C for 90 min under gentle stirring (300 rpm). During this aging process, the solution color gradually changed from brown to red, confirming the successful formation of pentatwinned defects. The resulting seed solution was stored at room temperature.

4.4.2 | Scaled-Up AuBipy Synthesis

The growth solution for AuBipy nanoparticles was prepared in a 1 L glass bottle by sequentially adding, under magnetic stirring (500 rpm), 275 mL of water, 250 mL of CTAB solution (0.2 M), 10 mL of $HAuCl_4$ (25 mM), 5 mL of $AgNO_3$ (10 mM), 0.833 mL of HCl (12 M), and 4 mL of ascorbic acid (0.1 M), all prepared in water. Upon the addition of ascorbic acid, the solution color changed from orange-yellow to colorless. Subsequently, 12 mL of pentatwinned seed solution was introduced, and the reaction mixture was maintained at 30°C for 2 h. After completion of the growth process, the resulting AuBipy nanoparticles were collected and washed three times with water to remove excess CTAB, and finally redispersed in a total volume of 10 mL of CTAB 0.16 mg mL^{-1}.

4.5 | PEGylation and Phase Transfer of Inorganic Nanoparticles

CTAB-free AuBipy nanoparticles exhibit a localized surface plasmon resonance (LSPR) band centered at approximately 808 nm, with a molar extinction coefficient of 3.63×10^{10} M^{-1} cm^{-1} at this wavelength. For PEGylation, a total of 500,000 MeO-PEG-SH chains per particle was considered. Initially, 1% of this amount (5,000 chains per particle) was added to the colloidal dispersion by introducing 75 µL of a MeO-PEG-SH solution (20 mg mL^{-1}) into 10 mL of an aqueous AuBipy dispersion (15 nM). In a separate container, 150 mg of MeO-PEG-SH, corresponding to the full coverage of 500,000 chains per particle, was dissolved in chloroform.

The aqueous nanoparticle dispersion and the PEG solution in chloroform were combined in a separatory funnel and vigorously shaken, followed by the addition of 10 mL of methanol to initiate phase transfer from the aqueous to the organic phase. The resulting emulsion was broken by the addition of excess water. Once transferred to the organic phase, the AuBipy nanoparticles were collected, dried under rotary evaporation, and redispersed in the same volume of N,N-dimethylformamide (DMF) as the initial aqueous dispersion.

Phase transfer of gold nanorods (AuNRs) was performed following the same protocol as for AuBipy, using a molar extinction coefficient of 4.90×10^9 M^{-1} cm^{-1}.

4.6 | Synthesis of AuNPs@NU-1000 Nanocomposites

In a 20 mL glass vial, a precursor solution was prepared by dissolving 64 mg of $ZrOCl_2 \cdot 8H_2O$ and 10 mg of H_4TBAPy in 9 mL of N,N-dimethylformamide (DMF). Subsequently, 1 mL of PEGylated Au nanoparticles (either bipyramids or nanorods) at the desired concentration was added, followed by the addition of acetic acid (2 mL) and water (1 mL). The vial was sealed and heated at 90°C for 30 min. After completion of the reaction, the product was collected by centrifugation at 7,200 rcf for 10 min, washed three times with DMF and three times with acetone, and finally dried under vacuum for further characterization.

4.7 | PEGylation of AuNPs@NU-1000 Nanocomposites

Surface modification of AuNPs@NU-1000 was performed using an MeO-PEG-PO_3 polymer. Briefly, the product obtained from a single synthesis of NU-1000 or AuNPs@NU-1000, dispersed in water, was mixed with 2.5 mL of an aqueous MeO-PEG-PO_3 solution (25 mg mL^{-1}). The mixture was stirred at 500 rpm for 3 h using a magnetic stir bar. Subsequently, the coated material was purified by three successive washing steps with water, each involving centrifugation at 10,000 rcf for 10 min.

4.8 | Cell Culture

Adenocarcinoma human alveolar basal epithelial cells (A549 cells, ATCC) were cultured in complete Dulbecco's Modified Eagle Medium (DMEM, high glucose (4.5 g L^{-1}) and pyruvate, Gibco, Thermo Fisher, Massachusetts, USA), supplemented with 10% fetal bovine serum (FBS, Gibco, Thermo Fisher, Massachusetts, USA) and Penicillin/Streptomycin (P/S, 50 U mL^{-1}–50 µg mL^{-1}) (Gibco, Thermo Fisher, Massachusetts, USA) (cDMEM) in a humidified chamber at 37°C under 5% CO_2. After reaching 80% confluency, the cells were washed with Dulbecco's phosphate-buffered saline (PBS, Thermo Fisher, Massachusetts, USA) and passaged after incubation with 0.25% Trypsin-EDTA (Gibco, Thermo Fisher, Massachusetts, USA).

4.9 | MTT Assay

MTT (3-[4,5-dimethylthiazol-2-yl]-2,5-diphenyltetrazolium bromide) assay was performed to study cell viability after the nanocomposite exposure. A549 cells were seeded in 96-well plates at a density of 7,500 cells per well in 100 µL of cDMEM. After 24 h, the medium was removed and replaced with 100 µL of nanocomposite solution diluted in fresh cDMEM, with final nanocomposite concentrations ranging from 1 to 200 pM. After 6 h, each well was rinsed once with 1X PBS, and 100 µL of freshly prepared MTT solution diluted in cDMEM was added. 96-well plates were left for 3 h at 37°C and 5% CO_2, then MTT solution was removed, and 50 µL of DMSO was added to each well to dissolve the formazan crystals. After 10 min at 37°C and 5% CO_2, absorbance was measured with a plate reader (TECAN, Infinite 200 PRO) at 540 nm. The absorbance value of each well provided by the instrument is an average of nine consecutive measurements in the same well. The final absorbance value for control cells (A_c) (untreated) is an average of at least nine different well values. Final absorbance values for samples (A_s) are a mean of three independent well values. Cell viability value is calculated as follows: $(A_s/A_c) \times 100$.

4.10 | Sample Preparation for Imaging Analysis

A549 cells were seeded in an Ibidi 8 Well chamber removable slide (#80841, Ibidi, Germany) at a concentration of 18,000 cells per well. After 24 h, the medium was removed and replaced with 100 µL of nanocomposite solution diluted in fresh cDMEM, with a final nanocomposite concentration of 100 pM. After 6 h, each well was washed three times with 1X PBS to eliminate non-internalized nanocomposites. Cells were then fixed with 3.6% paraformaldehyde (PFA, Sigma-Aldrich) in PBS for 15 min at room temperature. After fixation, the samples were washed three times with PBS. The removable chamber was detached according to the manufacturer's instructions, and the samples were kept in Ibidi Mounting Medium (Ibidi, Germany) for imaging analysis.

Author Contributions

M.C. carried out the synthesis and characterization of the materials; O.S. and E.K. conducted the scattering experiments. M.C., E.S. and P.d.P performed hyperspectral experiments and analysis. J.M.V.-F. performed the TEM characterization. T.M.C. and S.B. performed 3D electron tomography with in situ heating experiments. M.C., E.P., B.P., and P.d.P. designed the experiments and wrote the paper. E.P., B.P., and P.d.P. secured the funding necessary for this work. The manuscript was written with contributions from all authors, and all authors have approved the final version.

Acknowledgements

This work has received funding from the European Union's Horizon 2020 research H2020- FET-Open grant agreement no. 899612. The authors acknowledge the financial support of the European Research Council (starting grant #950421), the MCIN/AEI (PID2022-142338OB-I00, PID2023-152844NB-I00, PID2023-151448NB-I00; CNS2023-144318; TED2021-132522B-I00), and the Xunta de Galicia (ED431B2023/19, ED431F 2021/02, 2021-CP090, ED431C 2022/018, and Centro Singular de Investigación de Galicia Accreditation 2019–2022 #ED431G 2019/03). M.C. and T.M.C acknowledge H2020-MSCA-ITN grant agreement no. 860942. O.S. acknowledges the European Innovation Council project reaCtor, No. 101099405. J.M.V.-F. acknowledges support from Grant Number. RYC2023-045520-I, funded by the MCIU/AEI/10.13039/501100011033 and the FSE+. The authors are grateful for the use of RIAIDT-USC analytical facilities, particularly to Dr. Bruno Dacuña Mariño (Unidade de Raios X).

Conflicts of Interest

The authors declare no conflicts of interest.

Data Availability Statement

The data that support the findings of this study are available from the corresponding author upon reasonable request.

References

1. H. Li, M. Eddaoudi, M. O'Keeffe, and O. M. Yaghi, "Design and Synthesis of an Exceptionally Stable and Highly Porous Metal-Organic Framework," *Nature* 402 (1999): 276–279, https://doi.org/10.1038/46248.

2. S. S. Y. Chui, S. M. F. Lo, J. P. H. Charmant, A. G. Orpen, and I. D. Williams, "A Chemically Functionalizable Nanoporous Material $[Cu_3(TMA)_2\ (H_2O)_3]$(n)," *Science* 283 (1999): 1148–1150, https://doi.org/10.1126/science.283.5405.1148.

3. R. Freund, S. Canossa, S. M. Cohen, et al., "25 Years of Reticular Chemistry," *Angewandte Chemie—International Edition* 60 (2021): 23946–23974, https://doi.org/10.1002/anie.202101644.

4. J. R. Holst and A. I. Cooper, "Ultrahigh Surface Area in Porous Solids," *Advanced Materials* 22 (2010): 5212–5216, https://doi.org/10.1002/adma.201002440.

5. I. M. Hönicke, I. Senkovska, V. Bon, et al., "Balancing Mechanical Stability and Ultrahigh Porosity in Crystalline Framework Materials," *Angewandte Chemie—International Edition* 57 (2018): 13780–13783, https://doi.org/10.1002/anie.201808240.

6. O. K. Farha, I. Eryazici, N. C. Jeong, et al., "Metal–Organic Framework Materials with Ultrahigh Surface Areas: Is the Sky the Limit?," *Journal of the American Chemical Society* 134 (2012): 15016–15021, https://doi.org/10.1021/ja3055639.

7. H. Furukawa, N. Ko, Y. B. Go, et al., "Ultrahigh Porosity in Metal-organic Frameworks," *Science* 329 (2010): 424–428, https://doi.org/10.1126/science.1192160.

8. J. K. Schnobrich, K. Koh, K. N. Sura, and A. J. Matzger, "A Framework for Predicting Surface Areas in Microporous Coordination Polymers," *Langmuir* 26 (2010): 5808–5814, https://doi.org/10.1021/la9037292.

9. D. J. Tranchemontagne, J. L. Tranchemontagne, M. O'keeffe, and O. M. Yaghi, "Secondary Building Units, Nets and Bonding in the Chemistry of Metal–organic Frameworks," *Chemical Society Reviews* 38 (2009): 1257, https://doi.org/10.1039/b817735j.

10. H. Ghasempour, K.-Y. Wang, J. A. Powell, et al., "Metal–Organic Frameworks Based on Multicarboxylate Linkers," *Coordination Chemistry Reviews* 426 (2021): 213542, https://doi.org/10.1016/j.ccr.2020.213542.

11. Y. Bai, Y. Dou, L. H. Xie, W. Rutledge, J. R. Li, and H. C. Zhou, "Zr-based Metal–Organic Frameworks: Design, Synthesis, Structure, and Applications," *Chemical Society Reviews* 45 (2016): 2327–2367, https://doi.org/10.1039/C5CS00837A.

12. S. Tatay, S. Martínez-Giménez, A. Rubio-Gaspar, et al., "Synthetic Control of Correlated Disorder in UiO-66 Frameworks," *Nature Communications* 14 (2023): 1–12, https://doi.org/10.1038/s41467-023-41936-w.

13. I. del Castillo-Velilla, A. Sousaraei, I. Romero-Muñiz, et al., "Synergistic Binding Sites in a Metal-Organic Framework for the Optical Sensing of Nitrogen Dioxide," *Nature Communications* 14 (2023): 1–10, https://doi.org/10.1021/acsami.1c07701.

14. D. Nam, J. Kim, and W. Choe, "Evolution of Zr Nodes in Metal–organic Frameworks," *Trends in Chemistry* 5 (2023): 339–352, https://doi.org/10.1016/j.trechm.2023.02.009.

15. M. J. Hurlock, L. Hao, K. W. Kriegsman, X. Guo, M. O'Keeffe, and Q. Zhang, "Evolution of 14-Connected Zr6Secondary Building Units through Postsynthetic Linker Incorporation," *ACS Applied Materials & Interfaces* 13 (2021): 51945–51953, https://doi.org/10.1021/acsami.1c07701.

16. J. H. Cavka, S. Jakobsen, U. Olsbye, et al., "A New Zirconium Inorganic Building Brick Forming Metal-Organic Frameworks with Exceptional Stability," *Journal of the American Chemical Society* 130 (2008): 13850–13851, https://doi.org/10.1021/ja8057953.

17. J. E. Mondloch, W. Bury, D. Fairen-Jimenez, et al., "Vapor-Phase Metalation by Atomic Layer Deposition in a Metal–Organic Framework," *Journal of the American Chemical Society* 135 (2013): 10294–10297, https://doi.org/10.1021/ja4050828.

18. Z. Lu, J. Liu, X. Zhang, et al., "Node-Accessible Zirconium MOFs," *Journal of the American Chemical Society* 142 (2020): 21110–21121, https://doi.org/10.1021/jacs.0c09782.

19. W. Zeng, T. T. Y. Tan, Y. Benseghir, M. R. Reithofer, J. M. Chin, and J. Y. C. Lim, "Aerobic Photodegradation of Pyrene-Based Metal–Organic Framework NU-1000 to Terephthalic Acid," *Chemistry of Materials* 37 (2025): 3531–3541, https://doi.org/10.1021/acs.chemmater.5c00520.

20. R. Yu, L. M. Liz-Marzán, and F. J. García De Abajo, "Universal Analytical Modeling of Plasmonic Nanoparticles," *Chemical Society Reviews* 46 (2017): 6710–6724, https://doi.org/10.1039/C6CS00919K.

21. G. Mie, "Beiträge Zur Optik Trüber Medien, Speziell Kolloidaler Metallösungen," *Annalen der Physik* 330 (1908): 377–445, https://doi.org/10.1002/andp.19083300302.

22. Y. Peng, B. Xiong, L. Peng, H. Li, Y. He, and E. S. Yeung, "Recent Advances in Optical Imaging with Anisotropic Plasmonic Nanoparticles," *Analytical Chemistry* 87 (2015): 200–215, https://doi.org/10.1021/ac504061p.

23. Z. Gao, S. Shao, W. Gao, et al., "Morphology-Invariant Metallic Nanoparticles with Tunable Plasmonic Properties," *ACS Nano* 15 (2021): 2428–2438, https://doi.org/10.1021/acsnano.0c06123.

24. D. Jimenez de Aberasturi, A. B. Serrano-Montes, and L. M. Liz-Marzán, "Modern Applications of Plasmonic Nanoparticles: From Energy to Health," *Advanced Optical Materials* 3 (2015): 602–617, https://doi.org/10.1002/adom.201500053.

25. N. N. Zhang, M. Mychinko, S. Y. Gao, et al., "Self-Matching Assembly of Chiral Gold Nanoparticles Leads to High Optical Asymmetry and Sensitive Detection of Adenosine Triphosphate," *Nano Letters* 24 (2024): 13027–13036, https://doi.org/10.1021/acs.nanolett.4c03782.

26. A. Guglielmelli, F. Pierini, N. Tabiryan, C. Umeton, T. J. Bunning, and L. De Sio, "Thermoplasmonics with Gold Nanoparticles: A New Weapon in Modern Optics and Biomedicine," *Advanced Photonics Research* 2 (2021): 2000198, https://doi.org/10.1002/adpr.202000198.

27. K. R. Pulagam, M. Henriksen-Lacey, K. B. Uribe, et al., "In Vivo Evaluation of Multifunctional Gold Nanorods for Boron Neutron Capture and Photothermal Therapies," *ACS Applied Materials & Interfaces* 13 (2021): 49589–49601, https://doi.org/10.1021/acsami.0c17575.

28. J. Yi, E.-M. You, R. Hu, et al., "Surface-enhanced Raman Spectroscopy: A Half-century Historical Perspective," *Chemical Society Reviews* 54 (2024): 1453–1551, https://doi.org/10.1039/D4CS00883A.

29. J. Langer, D. Jimenez de Aberasturi, J. Aizpurua, et al., "Present and Future of Surface-Enhanced Raman Scattering," *ACS Nano* 14 (2020): 28–117, https://doi.org/10.1021/acsnano.9b04224.

30. J. W. M. Osterrieth and D. Fairen-Jimenez, "Metal–Organic Framework Composites for Theragnostics and Drug Delivery Applications," *Biotechnology Journal* 16 (2021): 1–14, https://doi.org/10.1002/biot.202000005.

31. G. Zheng, I. Pastoriza-Santos, J. Pérez-Juste, and L. M. Liz-Marzán, "Plasmonic Metal-Organic Frameworks," *SmartMat* 2 (2021): 446–465, https://doi.org/10.1002/smm2.1047.

32. B. Zhang, X. Cao, J. Wen, S. Guo, X. Duan, and X. M. Zhang, "Integration of Plasmonic Materials with MOFs/MOF-Derived Materials for Photocatalysis," *Coordination Chemistry Reviews* 518 (2024): 216113, https://doi.org/10.1016/j.ccr.2024.216113.

33. M. Cedrún-Morales, M. Ceballos, E. Polo, P. del Pino, and B. Pelaz, "Nanosized Metal–Organic Frameworks as Unique Platforms for Bioapplications," *Chemical Communications* 59 (2023): 2869–2887, https://doi.org/10.1039/D2CC05851K.

34. C. Carrillo-Carrión, R. Martínez, M. F. Navarro Poupard, et al., "Aqueous Stable Gold Nanostar/ZIF-8 Nanocomposites for Light-Triggered Release of Active Cargo inside Living Cells," *Angewandte Chemie* 131 (2019): 7152–7156, https://doi.org/10.1002/ange.201902817.

35. R. Martínez, C. Carrillo-Carrión, P. Destito, et al., "Core–shell Palladium/MOF Platforms as Diffusion-Controlled Nanoreactors in Living Cells and Tissue Models," *Cell Reports Physical Science* 1 (2020): 100076, https://doi.org/10.1016/j.xcrp.2020.100076.

36. C. Carrillo-Carrión, R. Martínez, E. Polo, et al., "Plasmonic-Assisted Thermocyclizations in Living Cells Using Metal–Organic Framework Based Nanoreactors," *ACS Nano* 15 (2021): 16924–16933, https://doi.org/10.1021/acsnano.1c07983.

37. Y. Liu, K. K. Chui, Y. Fang, S. Wen, X. Zhuo, and J. Wang, "Metal–Organic Framework-Enabled Trapping of Volatile Organic Compounds into Plasmonic Nanogaps for Surface-Enhanced Raman Scattering Detection," *ACS Nano* 18 (2024): 11234–11244, https://doi.org/10.1021/acsnano.4c00208.

38. X. Yang, Y. Liu, S. H. Lam, et al., "Site-Selective Deposition of Metal–Organic Frameworks on Gold Nanobipyramids for Surface-Enhanced Raman Scattering," *Nano Letters* 21 (2021): 8205–8212, https://doi.org/10.1021/acs.nanolett.1c02649.

39. M. Cedrún-Morales, M. Ceballos, E. Soprano, et al., "Light-Responsive Nanoantennas Integrated into Nanoscale Metal–Organic Frameworks for Photothermal Drug Delivery," *Small Science* 4 (2024): 2400088, https://doi.org/10.1002/smsc.202400088.

40. M. Ceballos, S. Funes-Hernando, G. Zampini, et al., "Seeded-Growth of PCN-224 Onto Plasmonic Nanoparticles: Photoactive Microporous Nanocarriers," *Small Structures* 5 (2024): 2300464, https://doi.org/10.1002/sstr.202300464.

41. S. Wang, Y. Chen, S. Wang, P. Li, C. A. Mirkin, and O. K. Farha, "DNA-Functionalized Metal–Organic Framework Nanoparticles for Intracellular Delivery of Proteins," *Journal of the American Chemical Society* 141 (2019): 2215–2219, https://doi.org/10.1021/jacs.8b12705.

42. M. Ceballos, M. Cedrún-Morales, M. Rodríguez-Pérez, et al., "High-Yield Halide-Assisted Synthesis of Metal–Organic Framework UiO-Based Nanocarriers," *Nanoscale* 14 (2022): 6789–6801, https://doi.org/10.1039/D1NR08305H.

43. A. Sánchez-Inglesias, N. Winckelmans, T. Altantzis, S. Bals, M. Grzelczak, and L. M. Liz-Marzán, "High-Yield Seeded Growth of Monodisperse Pentatwinned Gold Nanoparticles through Thermally Induced Seed Twinning," *Journal of the American Chemical Society* 139 (2017): 107–110, https://doi.org/10.1021/jacs.6b12143.

44. P. K. Verma, L. Huelsenbeck, and A. W. Nichols, "Controlling Polymorphism and Orientation of NU-901/NU-1000 Metal-Organic Framework Thin Films," in *AIChE Annual Meeting, Conference Proceedings*, 2022-Novem (2022), 10556–10565, https://doi.org/10.1021/acs.chemmater.0c03539.

45. J. W. M. Osterrieth, J. Rampersad, D. Madden, et al., "How Reproducible Are Surface Areas Calculated from the BET Equation?," *Advanced Materials* 34 (2022): 2201502, https://doi.org/10.1002/adma.202201502.

46. M. Shao, Y. Li, M. Chen, et al., "High-Efficiency Electrogenerated Chemiluminescence of Novel Zr-Based Metal–Organic Frameworks through Organic Linkers Regulation," *ChemElectroChem* 9 (2022): 202200866, https://doi.org/10.1002/celc.202200866.

47. T. M. Craig, A. A. Kadu, K. J. Batenburg, and S. Bals, "Real-time Tilt Undersampling Optimization during Electron Tomography of Beam Sensitive Samples Using Golden Ratio Scanning and RECAST3D," *Nanoscale* 15 (2023): 5391–5402, https://doi.org/10.1039/D2NR07198C.

48. T. M. Craig, R. Girod, G. Vinnacombe-Willson, L. M. Liz-Marzán, and S. Bals, "Towards Continuous Time-dependent Tomography: Implementation and Evaluation of Continuous Acquisition Schemes in Electron Tomography," *Ultramicroscopy* 277 (2025): 114207, https://doi.org/10.1016/j.ultramic.2025.114207.

49. P. Deria, J. Yu, T. Smith, and R. P. Balaraman, "Ground-State versus Excited-State Interchromophoric Interaction: Topology-Dependent Excimer Contribution in Metal–Organic Framework Photophysics," *Journal of the American Chemical Society* 139 (2017): 5973–5983, https://doi.org/10.1021/jacs.7b02188.

50. F. Gabriel, A. Roussey, S. S. Nobre, and A. Carella, "Pesticide Luminescent Detection and Degradation Using NU-1000 MOF," *Journal of Materials Chemistry C* 12 (2024): 11378–11385, https://doi.org/10.1039/D3TC04101H.

51. C. Chen and N. Hildebrandt, "Resonance Energy Transfer to Gold Nanoparticles: NSET Defeats FRET," *TrAC—Trends in Analytical Chemistry* 123 (2020): 115748, https://doi.org/10.1016/j.trac.2019.115748.

52. C. S. Yun, A. Javier, T. Jennings, et al., "Nanometal Surface Energy Transfer in Optical Rulers, Breaking the FRET Barrier," *Journal of the American Chemical Society* 127 (2005): 3115–3119, https://doi.org/10.1021/ja043940i.

53. W. Hao, G. Huang, G. Jiang, S. A. A. Dauda, and F. Pi, "Direct Phoxim Sensing Based on Fluorescent Metal-organic Framework of Nu-1000 Induced FRET," *Food Bioscience* 55 (2023): 102967, https://doi.org/10.1016/j.fbio.2023.102967.

54. X. Chen, Y. Zhuang, N. Rampal, et al., "Formulation of Metal–Organic Framework-Based Drug Carriers by Controlled Coordination of Methoxy PEG Phosphate: Boosting Colloidal Stability and Redispersibility," *Journal of the American Chemical Society* 143 (2021): 13557–13572, https://doi.org/10.1021/jacs.1c03943.

55. J. Mosquera, D. Wang, S. Bals, and L. M. Liz-Marzán, "Surfactant Layers on Gold Nanorods," *Accounts of Chemical Research* 56 (2023): 1204–1212, https://doi.org/10.1021/acs.accounts.3c00101.

56. A. Rabbani, R. Rudacille, and K. Hasegawa, "Local Refractive Index Sensitivity of Localized Surface Plasmon Resonance Biosensors," *The Journal of Physical Chemistry C* 128 (2024): 19210–19221, https://doi.org/10.1021/acs.jpcc.4c03456.

57. C. Nhung, Z. Ouzit, C. Lethiec, et al., "Polarimetric Dark-field Spectroscopy of Gold Bipyramids : Measuring Single Particle 3D Orientation," *Optics Communications* 510 (2022): 127947, https://doi.org/10.1016/j.optcom.2022.127947.

58. C. Fang, G. Zhao, Y. Xiao, J. Zhao, Z. Zhang, and B. Geng, *Facile Growth of High-Yield Gold Nanobipyramids Induced by Chloroplatinic Acid for High Refractive Index Sensing Properties* (Nature Publishing Group, London, 2016), 1–8.

59. T. H. Chow, N. Li, X. Bai, X. Zhuo, L. Shao, and J. Wang, "Gold Nanobipyramids: An Emerging and Versatile Type of Plasmonic Nanoparticles," *Accounts of Chemical Research* 52 (2019): 2136–2146, https://doi.org/10.1021/acs.accounts.9b00230.

60. S.-Y. Ding, J. Yi, J.-F. Li, et al., "Nanostructure-based Plasmon-Enhanced Raman Spectroscopy for Surface Analysis of Materials," *Nature Reviews Materials* 1 (2016): 16021, https://doi.org/10.1038/natrevmats.2016.21.

61. S. T. Sivapalan, B. M. DeVetter, T. K. Yang, et al., "Off-resonance Surface-Enhanced Raman Spectroscopy from Gold Nanorod Suspensions as a Function of Aspect Ratio: Not What We Thought," *ACS Nano* 7 (2013): 2099–2105, https://doi.org/10.1021/nn305710k.

62. P. Z. El-Khoury, "Tip-Enhanced Raman Chemical and Chemical Reaction Imaging in H_2O with Sub-3-nm Spatial Resolution," *Journal of the American Chemical Society* 145 (2023): 6639–6642, https://doi.org/10.1021/jacs.3c01626.

63. E. Polo, V. Araban, B. Pelaz, et al., "Photothermal Effects on Protein Adsorption Dynamics of PEGylated Gold Nanorods," *Applied Materials Today* 15 (2019): 599–604, https://doi.org/10.1016/j.apmt.2019.04.013.

Supporting Information

Additional supporting information can be found online in the Supporting Information section.

Supporting File:1: smll75289-sup-0001-SuppMat.docx.

Supporting File:2: smll75289-sup-0002-VideoS1.mp4.

Supporting File:2: smll75289-sup-0003-VideoS2.mp4.

Supporting File 3: smll75289-sup-0004-VideoS3.mp4.

Supporting File 4: smll75289-sup-0005-VideoS4.mp4